Geophysical Research Letters

RESEARCH LETTER
10.1029/2025GL115218

Unzipping of the Conjugate Fault System During the 2024 Mw7.4 Hualien Earthquake

Liuwei Xu[1], Lingsen Meng[1], Wenbin Xu[2], Yen-Yu Lin[3,4,5], Jianghui Geng[6], Saeed Mohanna[1], and Grant Kawamoto[1]

[1]Department of Earth, Planetary, and Space Sciences, University of California Los Angeles, Los Angeles, CA, USA, [2]School of Geosciences and Info-Physics, Central South University, Changsha, China, [3]Department of Earth Sciences, National Central University, Taoyuan, Taiwan, [4]Earthquake-Disaster & Risk Evaluation and Management Center, National Central University, Taoyuan, Taiwan, [5]Graduate Institute of Applied Geology, National Central University, Taoyuan, Taiwan, [6]State Key Laboratory of Precision Geodesy, APM, Chinese Academy of Sciences, Wuhan, China

Key Points:

- We imaged the rupture process and constructed the slip model of the 2024 Hualien earthquake
- The mainshock happened on the east-dipping Longitudinal Valley Fault and its west-dipping conjugate fault
- The complex fault system played a critical role in accommodating the strain accumulation caused by the plate collision

Supporting Information:

Supporting Information may be found in the online version of this article.

Correspondence to:

L. Meng,
lsmeng@g.ucla.edu

Citation:

Xu, L., Meng, L., Xu, W., Lin, Y.-Y., Geng, J., Mohanna, S., & Kawamoto, G. (2025). Unzipping of the conjugate fault system during the 2024 Mw7.4 Hualien earthquake. *Geophysical Research Letters*, *52*, e2025GL115218. https://doi.org/10.1029/2025GL115218

Received 4 FEB 2025
Accepted 17 JUN 2025

Author Contributions:

Conceptualization: Liuwei Xu, Lingsen Meng
Data curation: Wenbin Xu, Jianghui Geng
Formal analysis: Liuwei Xu, Grant Kawamoto
Funding acquisition: Lingsen Meng
Investigation: Liuwei Xu
Methodology: Liuwei Xu, Lingsen Meng, Wenbin Xu, Jianghui Geng, Saeed Mohanna
Project administration: Lingsen Meng
Resources: Yen-Yu Lin
Software: Liuwei Xu, Lingsen Meng, Wenbin Xu, Jianghui Geng
Supervision: Lingsen Meng
Validation: Liuwei Xu, Yen-Yu Lin, Grant Kawamoto
Visualization: Liuwei Xu

Abstract On 2 April 2024, a Mw7.4 earthquake struck Taiwan's eastern coast near Hualien City. The fault responsible for the mainshock remained under debate due to the region's complex plate boundary system and intricate fault interactions. To determine the fault plane and resolve the rupture process, we analyzed local and teleseismic waveform recordings, along with near-field and satellite geodetic data. We employed Slowness-Enhanced Back-Projection and Finite Fault Inversion techniques across seismic and geodetic data sets. Our analysis revealed that the rupture propagated on the east-dipping Longitudinal Valley Fault (LVF) and its west-dipping conjugate fault. The rupture started on the LVF and reached the conjugate fault at ~8 s, after which slip occurred simultaneously on both faults. The aftershock distribution validated the fault geometry. The 2024 mainshock demonstrated the seismic potential of the LVF and its role in accommodating the thrust component of strain accumulation from the plate collision near Hualien.

Plain Language Summary On 2 April 2024, a magnitude 7.4 earthquake struck near Hualien City on Taiwan's east coast. Scientists were unsure which fault caused the earthquake because the area has a complex system of interacting faults. To investigate, we analyzed seismic waves recorded by local and global seismic stations, as well as ground movement measured by satellites and local GPS stations. Our results showed that the earthquake happened on two connected faults: the east-dipping Longitudinal Valley Fault (LVF) and a west-dipping fault beneath the hypocenter. The rupture started on the LVF and reached the intersection of two faults at ~8 s, after which slip occurred simultaneously on both planes. Aftershocks that followed the main quake also aligned with this fault system, confirming our findings. This earthquake highlighted that the LVF and its connected fault were capable of producing large earthquakes, making it an important fault system to monitor for future seismic hazards in the region.

1. Introduction

On 2 April 2024, the eastern coast of Taiwan experienced one of the most significant seismic events in its recent history, the Mw7.4 Hualien earthquake (Figure 1a). The earthquake caused extensive damage to buildings, roads, and local infrastructure, severely disrupting daily life and economic activities (Stein et al., 2024). Taiwan's position at the boundary between the Philippine Sea Plate (PSP) and the Eurasian Plate (EUP) makes it one of the most tectonically complex and active regions in the world. The convergence rate between two plates near the earthquake site is ~30 mm/year (Hsu et al., 2009). The Longitudinal Valley, situated along the convergence of the PSP and the EUP, has a well-documented history of seismic activity. Notable historical earthquakes beneath or near the valley include the 2003 Mw6.8 Chengkung earthquakes (Ching et al., 2007; Hu et al., 2007), the 2018 Mw6.4 Hualien earthquake (Huang & Huang, 2018; Lee et al., 2019), and the 2022 Mw6.5 and Mw6.9 Chishang earthquake doublet (Yang et al., 2024) (Figure 1a). Beneath the Longitudinal Valley, two primary faults dominate the seismic activity in the region: the east-dipping Longitudinal Valley Fault (LVF) and the west-dipping Central Range Fault (CRF) (Figure 1c). Given their close proximity and historical records indicating both faults' potential to generate large earthquakes, several questions arise: What roles do the LVF and CRF play in accommodating the strain accumulation from the PSP-EUP collision? Do they exhibit differences in seismic activity? Are there any previously undocumented faults involved in the 2024 mainshock? Furthermore, the LVF places the ocean side on the hanging wall, whereas the CRF positions Taiwan island as the hanging wall. Stronger ground accelerations

Writing – original draft: Liuwei Xu, Lingsen Meng, Wenbin Xu, Yen-Yu Lin, Saeed Mohanna
Writing – review & editing: Liuwei Xu, Lingsen Meng, Wenbin Xu, Yen-Yu Lin, Jianghui Geng, Saeed Mohanna, Grant Kawamoto

typically occur on the hanging wall side during reverse-slip earthquakes (Abrahamson & Somerville, 1996), underscoring the importance of assessing the tsunami and island seismic risks associated with each fault. The 2024 Mw7.4 Hualien earthquake offers a valuable opportunity for seismologists to investigate fault behaviors, providing important insights for future hazard risk predictions and mitigation strategies in this tectonically active region.

In this study, we employed advanced seismic analysis techniques, including Slowness-Enhanced Back-Projection (SEBP; Meng et al., 2016) and joint Finite Fault Inversion (FFI; Ji et al., 2002, 2003), to identify the fault system responsible for the mainshock and investigate the earthquake's rupture kinematics. We utilized the fairfield and local seismic data, as well as the coseismic ground deformation measured by Global Navigation Satellite System (GNSS) stations and Interferometric Synthetic Aperture Radar (InSAR) satellites to reveal how the rupture propagated across the fault plane. To further validate our resolved fault geometry, we relocated 2,011 aftershocks that occurred in 1 week following the mainshock. Additionally, we integrated the mainshock slip distribution with historical seismicity patterns to compare activity on the LVF and CRF, and discussed the LVF's role in accommodating plate convergence.

2. Data and Methods

2.1. Joint Finite Fault Inversion

FFI is a technique used to model the slip distribution and rupture propagation along faults during an earthquake. Our application of the FFI method involved an integrated approach (Text S1 in Supporting Information S1; Ji et al., 2002, 2003), combining near-field strong motion records (Figures S1 and S2 in Supporting Information S1), broadband teleseismic waveforms (Figures S3–S6 in Supporting Information S1), static GNSS data (Figure S7, Text S2, and Table S1 in Supporting Information S1), and InSAR line-of-sight displacement data (Figures S8, S9, Text S3, and Table S2 in Supporting Information S1). Detailed processing of the data sets can be found in Texts S1–S3 of Supporting Information S1. In our joint FFI, the hypocenter was set at (121.58°E, 23.86°N, 22.52 km depth), as relocated by Central Weather Administration (CWA, 2012). The US. Geological Survey (USGS) identified two moment tensor nodal planes as the candidate of the fault. We tested several fault geometries and adopted a conjugate fault system as the preferred fault geometry (Figure 2), as it provided the best fit to the teleseismic P waves and yielded smallest misfits across all seismic and geodetic data sets (see Sections 3.1 and 4.1 for more discussions on optimal fault planes searching). The conjugate fault model consisted of two intersecting faults (Figure 2, Table S3 in Supporting Information S1). The first was an east-dipping plane (Segment 1 in Figures 2a and 2b) with a strike of 23° and a dip of 67°, consistent with the geometry of the LVF, and it hosted the hypocenter. The second was a west-dipping plane (Segment 2 in Figures 2a and 2b), located beneath the hypocenter, with a strike of 203° and a dip of 40°. These two planes intersected at ∼32 km depth. We used the simulated annealing technique to explore a range of possible fault slip distributions, rupture initiation time, the shape of slip rate function, and the rake angle on each subfault (Ji et al., 2002, 2003). Green's functions for local strong motion waveforms and static displacements are computed using the f-k approach (Zhu & Rivera, 2002) and the 1-D crust model by Huang et al. (2014) (Table S4 in Supporting Information S1).

2.2. Slowness-Enhanced Back-Projection

BP is an earthquake source imaging technique used to visualize the high-frequency (HF) radiator propagation during the earthquake. The technique utilizes the waveforms recorded by large and dense networks at teleseismic distances ($30° < \Delta < 90°$) (Ishii et al., 2005; Kiser & Ishii, 2017). The SEBP method builds on MUltiple SIgnal Classification (MUSIC) BP (Meng et al., 2011) by incorporating adjustments for the slowness of seismic waves—that is, the temporal delay per unit distance as waves travel through various materials in the Earth's crust (Meng et al., 2016; Zhang, 2019).

For the 2024 Hualien earthquake, we collected seismic data from three arrays: the USArray in Alaska (AK, Figures S10 and S11 in Supporting Information S1), Australian networks (AU, Figures S11 and S12 in Supporting Information S1), and European networks (EU, Figure 1; Figures S11 and S13 in Supporting Information S1). We downloaded the vertical component of broadband seismograms. All waveforms were first aligned based on the P phase travel times predicted by a 1-D reference Earth model. The remaining time errors between the predicted and actual P arrivals are calculated and corrected by cross-correlating the first 10-s waveforms centered on the P arrivals (5-s before and 5-s after; Meng et al., 2011). Aligned waveforms were then bandpass filtered to 0.5–2 Hz

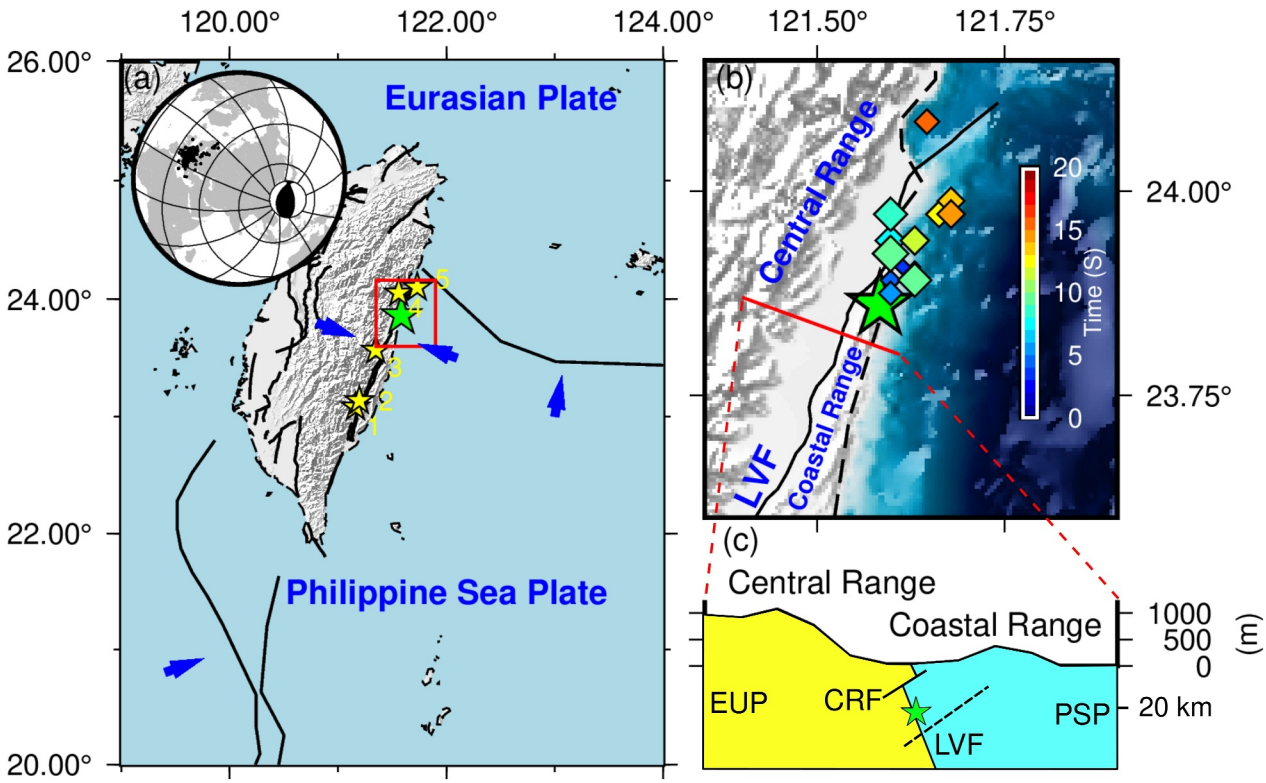

Figure 1. Tectonic map and BP results. (a) The tectonic map and the source region in (b) (red box). The upper inset shows the Europe array used for BP. The green star denotes the 2024 mainshock epicenter. Yellow stars denote major earthquakes at Longitudinal Valley since 2010. Events 1 and 2: the 2022 Mw6.5 and Mw6.9 Chishang earthquake doublet. Event 3: the 2013 Mw6.2 Ruisui earthquake. Event 4: the 2019 Mw6.2 Hualien earthquake. Event 5: the 2018 Mw6.4 Hualien earthquake. Blue arrows indicate the plate subduction or collision directions. (b) BP results. The colored symbols denote high-frequency radiators imaged by Europe array. The symbol size is proportional to the BP power and the color represents the rupture time. The red line indicates the location of the cross-section shown in (c). (c) Sketch of fault system in eastern Taiwan. The configurations of the CRF, shallow LVF, deep LVF, and the offset between them are adapted from Huang and Wang (2022). The black dashed line indicates the conjugate fault of the LVF ruptured during the 2024 mainshock.

to enhance the resolution while keeping enough signal-to-noise ratio. We back-projected the filtered seismic waveforms to their hypothesized source locations and imaged the subsequent HF radiators using the differential travel time relative to the mainshock hypocenter, with a sliding time window of 1-s. Finally, the slowness correction terms were computed using 3–5 aftershocks' locations given by Taiwan CWA catalog (Table S5 in Supporting Information S1). For a set of aftershocks, we applied the same travel time corrections to them as the mainshock, and the distance between the BP-inferred and catalog aftershock locations were utilized to compute the slowness correction terms (Meng et al., 2016; Zhang, 2019). This step enables a more accurate depiction of the rupture propagation. Table S5 in Supporting Information S1 shows the aftershock locations imaged by BP before and after the slowness correction, and compares them with the CWA catalog locations. The root-mean-square of aftershock locating errors reduced from ∼8 to ∼3 km. Figure 1b; Figures S10–S13 in Supporting Information S1, and Movies S1–S3 show the final images produced by SEBP which provide detailed visualizations of the HF radiators during the mainshock.

3. Results

3.1. Optimal Fault Plane Searching

In our study, a critical aspect of finite fault modeling was identifying the optimal fault geometry. We first searched for the optimal fault based on the east dipping nodal plane resolved by the USGS. By examining teleseismic, local strong motion, GNSS, and InSAR data, we aimed to optimize the fault strike and dip angles for enhanced model fidelity. Figure S14a in Supporting Information S1 illustrates the variation in data fitting residuals when the dip angle was fixed at 65° and the strike angle was varied within a range of 10°–30°. Figure S14b in Supporting Information S1 shows the search for the optimal fault dip, with the strike angle fixed at the optimal value of 23°

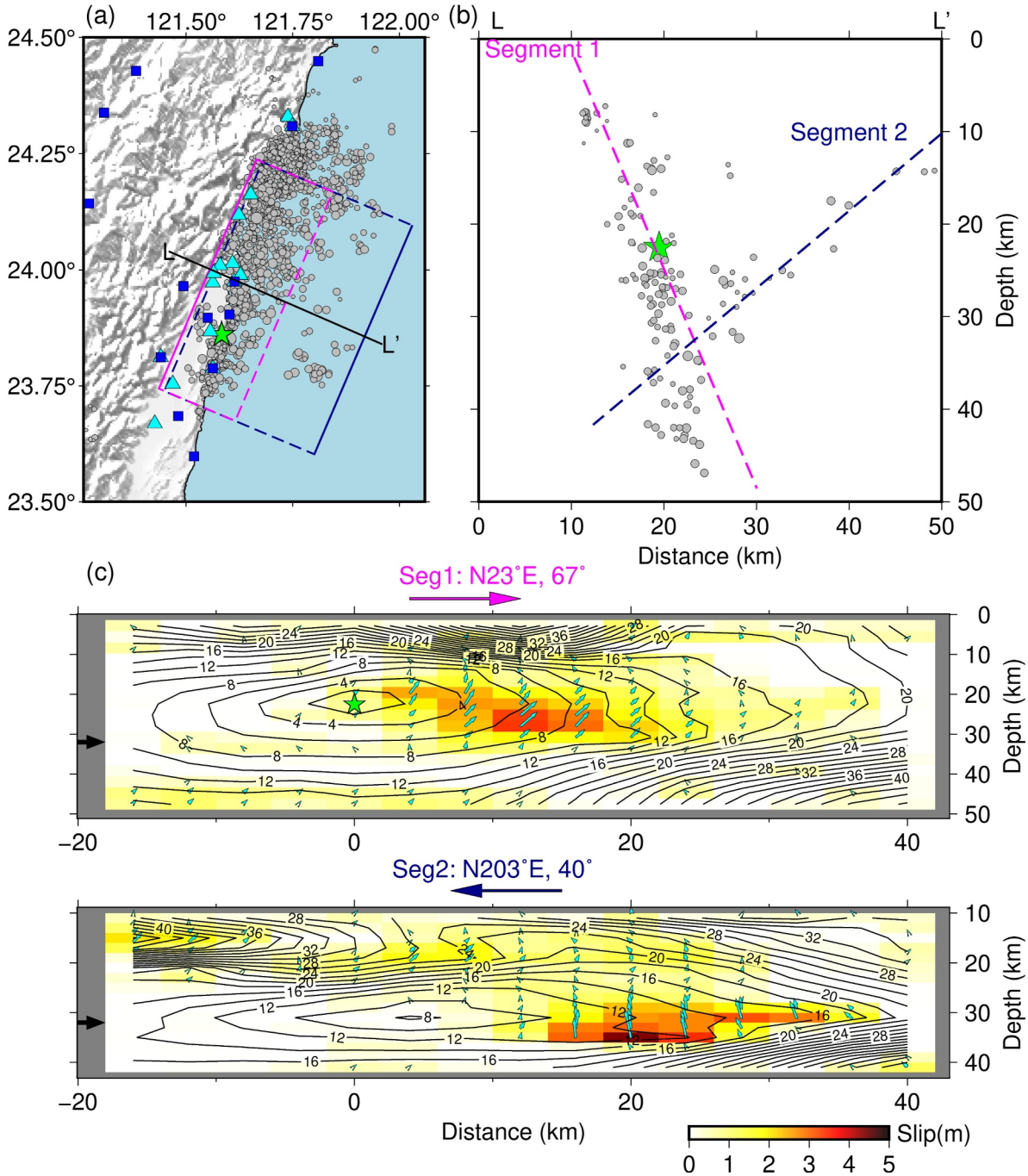

Figure 2. FFI results. (a) Map view of the fault plane. The magenta and blue boxes denote the fault planes adopted in FFI, with the solid lines denoting the upper boundaries of the planes. The green star denotes the hypocenter. The cyan triangles denote the local strong motion stations used in FFI. The blue squares denote the GNSS stations used in FFI. The gray dots denote the aftershocks within 1 week following the mainshock. (b) Vertical cross-section views of seismicity along line LL′ indicated in (a), within 5 km distance to the line. The dashed lines in (b) denote the fault planes adopted in our finite fault inversion. (c) Spatial distribution of final slip (colors), rupture initiation time (contours), and slip direction (rake angle, cyan arrows). The strike and dip of each fault segment are annotated above the respective fault planes. The black arrows on the left indicate the intersection of two faults.

(from Figure S14a in Supporting Information S1) while varying the dip angle from 55° to 70°. Ultimately, the misfit to all data sets was minimized with a strike angle of 23° and a dip angle of 67°. The strike angle aligned with the orientation of the Longitudinal Valley and the LVF (Styron & Pagani, 2020), while the dip angle was notably steep for a thrust fault.

However, upon detailed inspection of the teleseismic P waveforms, we found that a positive pulse occurring between 10 and 20 s could not be well reproduced at stations located between azimuths 22° and 184° (Figure S15 in Supporting Information S1). We also tested a flatter east-dipping fault with a dip angle of 55° (Figure S16 in Supporting Information S1). While this model better reproduced the 10–20 s pulses, it failed to capture the initial pulse between 0 and 10 s at stations within the 243°–335° azimuth range. This systematic misfit pattern suggests the involvement of a more complex fault structure during the mainshock. We examined the 1-week aftershock distribution and identified a possible west-dipping conjugate fault beneath the hypocenter (Figure 2b; Figures S17 and S18 in Supporting Information S1). This structure is evident in both the original CWA catalog and our relocated aftershock catalog (Figures S17 and S18 in Supporting Information S1; see Text S4 in Supporting Information S1 for more details about aftershock relocation). Based on this observation, we constructed a conjugate fault system by adding a west-dipping plane to the LVF (Figure 2b). The corresponding fault parameters are listed in Table S3 in Supporting Information S1. Incorporating the west-dipping fault significantly improved waveform fits for the teleseismic P phase (Figure S3 in Supporting Information S1) and reduced misfits for the geodetic and seismic data sets (Figure S19 in Supporting Information S1). Thus, we adopt the conjugate fault system as our preferred rupture scenario and base subsequent analyses and discussions on this configuration.

3.2. Rupture Kinematics

The earthquake initiated on the LVF and first propagated north-northeast and downward. At ∼8 s, the rupture front reached the intersection of the LVF and the west-dipping fault (Figure 2c; hereinafter referred to as "the conjugate fault"). Subsequently, slip developed simultaneously on both faults. On the LVF, the major slip occurred between 0 and 22 km along strike and 18–32 km in depth. The peak slip amplitude was ∼3.4 m, with reverse faulting accompanied by a moderate left-lateral strike-slip component (Figure 2c). On the conjugate fault, the main slip patch was distributed between 15 and 35 km along strike and 28–36 km in depth. The peak slip reached ∼4.4 m, and the mechanism was predominantly reverse with a minor strike-slip component. The seismic moment release was partitioned between the LVF and the conjugate fault, accounting for 47% and 53% of the total, respectively. HF radiators imaged using SEBP from the European array were generally consistent with the rupture process derived from the joint FFI (Figure S20 in Supporting Information S1 and Movie S4): the HF radiators were located at similar along-strike distances and coincided temporally with subfaults exhibiting substantial slip. After ∼16 s, no HF radiators were observed in the source region, likely due to reduced moment release during the later stage of the rupture. The average rupture speed inferred from SEBP was ∼1.4 km/s (Figure S21 in Supporting Information S1).

The total seismic moment derived from FFI was 1.38×10^{20} N·m, corresponding to a moment magnitude of Mw7.36. Most of the moment release occurred within the first 20 s (Figure S22 in Supporting Information S1). Our preferred rupture model reproduces the static displacements observed by GNSS and InSAR well (Figures S7 and S8 in Supporting Information S1). It also fits most strong-motion recordings (Figures S1 and S2 in Supporting Information S1). Some mismatches occur in the horizontal components at stations F019, F028, and F051, particularly in the later parts of the records. These discrepancies likely arise from site amplification effects due to soft sediments in the Hualien Plain (Kuo et al., 2018), which could not be accurately modeled using the simple 1-D velocity model adopted in FFI.

4. Discussion

4.1. The Fault System Responsible for the Mainshock

The fault system responsible for the Mw7.4 Hualien earthquake has presented a significant enigma, compounded by the complex regional tectonics. There was considerable debate regarding whether the earthquake occurred on the east-dipping LVF (Zheng et al., 2024), or the west-dipping CRF (Qiu et al., 2024; Tang et al., 2024), or a composite system involving multiple faults (Cheloni et al., 2024). We found that local GNSS recordings revealed a distinct vertical movement transition: coastal stations east of the LVF exhibited uplift (stations NDHU, SHUL; Figure S23b in Supporting Information S1), while stations to the west and further inland showed subsidence (TUNM, DNFU; Figure S23b in Supporting Information S1). This transition is characteristic of reverse faulting on an east-dipping plane, with the fault's upper boundary passing through the valley between these stations. However, as discussed in Section 3.1, a single east-dipping fault failed to reproduce the observed teleseismic P waveforms, motivating the construction of a conjugate fault system. The observed GNSS deformation pattern was

also well reproduced by the conjugate fault model (Figure S7 in Supporting Information S1), supporting its validity as the preferred rupture scenario.

We also performed three additional inversions using complex fault geometries informed by recent studies (Cheloni et al., 2024; Zheng et al., 2024): (a) a two-segment model composed of a deep, east-dipping segment with a strike of 23° and dip of 67°, and a shallow, west-dipping segment with a strike of 203° and dip of 30° (Figures S24 and S25 in Supporting Information S1). These geometries correspond to the LVF and CRF, respectively, and we refer to this configuration as the "LVF&CRF model" hereafter; (b) a listric east-dipping fault model consisting of a steep (67°) segment above the hypocenter and a flatter (54°) segment below it (Figure S26 in Supporting Information S1); and (c) a single west-dipping fault adopting the strike and dip of the other nodal plane (strike = 218°, dip = 40°) provided by the USGS (Figure S27 in Supporting Information S1). The LVF&CRF model failed to reproduce the positive pulse between 10 and 20 s at stations located to the east of the source (Figure S28 in Supporting Information S1), a limitation also observed in the single-plane east-dipping model, likely due to the concentration of slip on the deep LVF (Figure S24 in Supporting Information S1). The listric model did not capture the initial pulse between 0 and 10 s at stations spanning azimuths 216°–335° (Figure S29 in Supporting Information S1). Additionally, both the LVF&CRF and listric models produced substantial misfits in the horizontal components at GNSS stations TUNM, HUA3, and YNEL (Figures S24a and S30a in Supporting Information S1). Both models underestimated the eastward displacements, whereas the preferred conjugate model accurately reproduced the observed eastward deformation (Figure S7a in Supporting Information S1). This discrepancy arises from the lack of significant slip on the CRF in the LVF&CRF model, and the complete absence of a west-dipping fault in the listric model. The single west-dipping fault model resulted in large misfits to the teleseismic P waveforms (Figure S31 in Supporting Information S1) and predicted uplift at station TUNM, inconsistent with the observed subsidence (Figure S32b in Supporting Information S1). Moreover, all three models yielded significant misfits to the seismic and geodetic data sets (Figure S19 in Supporting Information S1) and were therefore not considered viable representations of the rupture process.

To further validate the fault plane in our preferred model, we collected the information of aftershocks occurring within 1 week following the mainshock from Taiwan Seismological and Geophysical Data Management System (GDMS) of CWA (Text S4 in Supporting Information S1). The smallest local magnitude (M_L) in the catalog was 0.82. We obtained the reference catalog and P and S wave arrival times from GDMS, and used the hypocenter double-difference earthquake location algorithm (HypoDD; Waldhauser & Ellsworth, 2000) to relocate the hypocenters for 2,011 aftershocks, as shown in Figures 2 and 3; Figures S17 and S18 in Supporting Information S1. The aftershock distribution, both before and after relocation, aligned well with the preferred model, supporting its validity (Figures S17 and S18 in Supporting Information S1).

4.2. Seismic Potential of the LVF

The Mw7.4 Hualien earthquake is the first extensively recorded Mw ≥ 7 event on the LVF with modern instrumentation. This event presents a valuable opportunity to investigate the seismic potential of the LVF and its role in accommodating plate collision in eastern Taiwan. The east coast and its adjacent offshore regions are seismically active, with more than 10 $M \geq 6$ events recorded since 2000 (Figure S23a in Supporting Information S1). The activity is influenced by the CRF and LVF and some minor faults (e.g., Meilun fault) under the valley. Along the Longitudinal Valley, M6 earthquakes have been observed on both sides of the valley, whereas M7 events have occurred exclusively on its eastern side. For instance, an Mw7.4 (Ms7.8) event in 1986 occurred offshore near Hualien City (Hwang & Kanamori, 1989; Zheng et al., 1995). Further back, an M_L7.3 strike-slip earthquake struck the offshore region in 1951 (Chen et al., 2008; Cheng et al., 1997; Jian & Wang, 2022; Shyu et al., 2007), followed by eight M_L6 and three M_L7 events rupturing multiple strike-slip and reverse-slip faults in the same year. Because the 1986 earthquake was also a reverse-slip event with a focal mechanism similar to the 2024 mainshock, we plotted its hypocenter and focal mechanism in Figures 3a and 3e. One of the nodal planes align with the west-dipping conjugate fault identified in our study. However, due to the large hypocentral uncertainty associated with sparse local station coverage at the time (Hwang & Kanamori, 1989; Lo et al., 2013; Shyu et al., 2007; Zheng et al., 1995), it remains ambiguous whether the 1986 event ruptured the conjugate fault or other offshore faults. Consequently, before the 2024 Mw7.4 earthquake, it was unclear whether the LVF could host $M \geq 7$ events. The 2024 mainshock confirms the seismic potential of the LVF and its conjugate fault, highlighting the need for updated seismic hazard evaluations and corresponding mitigation strategies for Hualien and nearby cities. The focal mechanisms of the 2024 and historical large earthquakes align

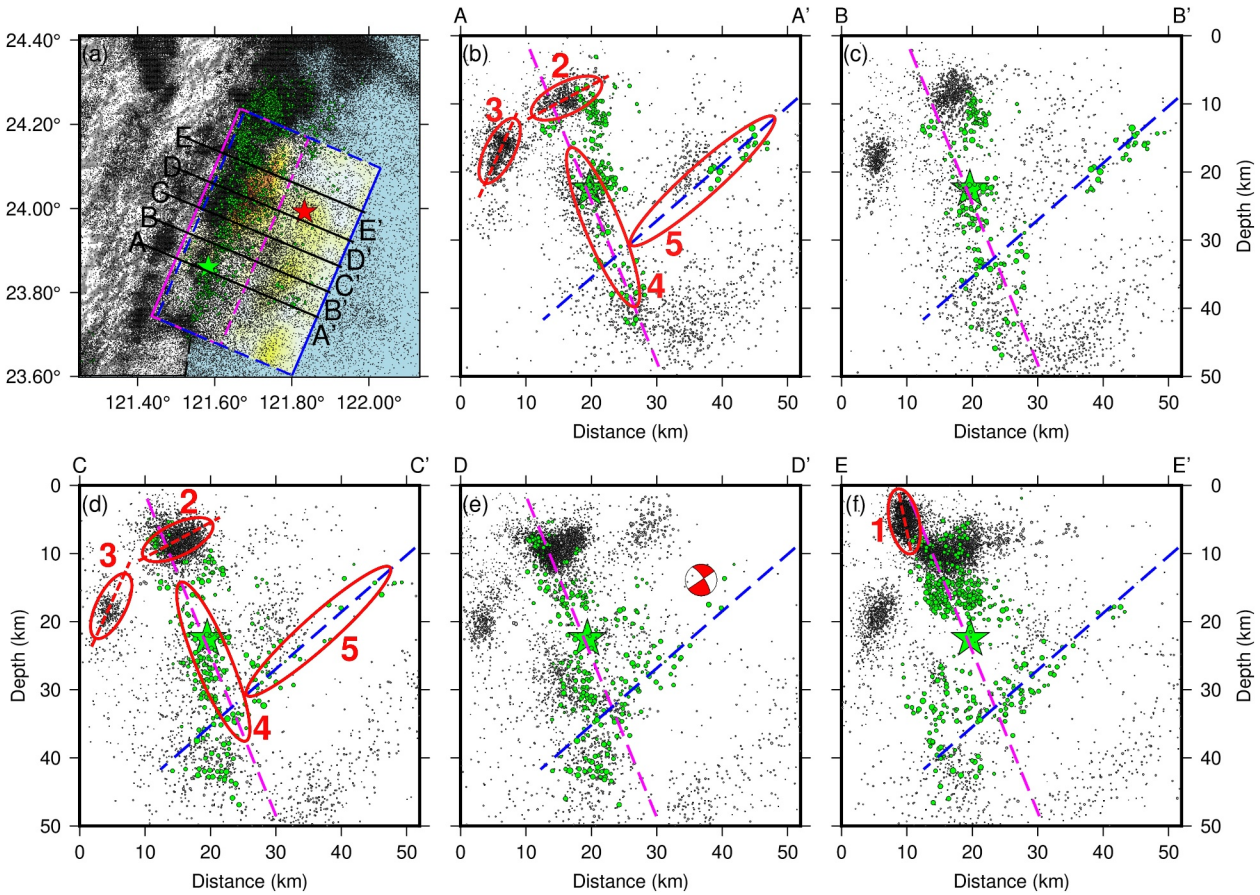

Figure 3. Seismicity distribution. (a) Seismicity and slip model. Black dots represent seismic events between 1990 and 2020, relocated by National Taiwan University. Green dots denote aftershocks occurring within 1 week following the 2024 mainshock, relocated in this study. The red star denotes the 1986 Ms7.8 event (Hwang & Kanamori, 1989). The green star denotes the 2024 mainshock. Black lines indicate the cross-sections shown in (b–f). (b) Vertical cross-section view of seismicity along line AA′ indicated in (a), within 2 km distance to the line. The magenta and blue dashed lines in (b) denote the fault planes adopted in our FFI. The red open ellipses and numbers (1–5) indicate the seismicity clusters. The red dashed lines indicate roughly fitted fault planes. (c) The same as (b) but for line BB′. (d) The same as (b) but for line CC′. (e) The same as (b) but for line DD′. The red beach ball denotes the focal mechanism of the 1986 Ms7.8 event. (f) The same as (b) but for line EE′.

with previous findings that the oblique collision zone between the PSP and the EUP in eastern Taiwan involves both strike-slip and thrust-faulting components (Jian et al., 2022; Kao et al., 1998). The occurrence of the 2024 mainshock suggests that the LVF and the offshore conjugate fault play a crucial role in accommodating the thrust component of strain and stress accumulation from the PSP-EUP collision, while offshore strike-slip faults, like those involved in the 1951 sequence, may release the strike-slip component.

The CRF and LVF also exhibit distinct background seismicity rates. Figure 3 provides a map view and cross-sectional perspective of all seismic events relocated by National Taiwan University (NTU) between 1990 and 2020 (Wu et al., 2013). The shallow, west-dipping CRF has exhibited a higher activity level, featuring denser clusters of seismicity (Figure 3) and four moderate (M6) events since 2000 near the Hualien city (Figure S23a and Table S6 in Supporting Information S1). At depths shallower than 25 km, three dense seismicity clusters (Groups 1–3 in Figure 3) are readily identifiable. Group 1 is associated with a steep fault linked to the 2018 Hualien earthquake sequence (Huang & Wang, 2022; Lo et al., 2019). Groups 3 and 2, attributed to the CRF and its branches (Huang & Wang, 2022), display different dip angles and are separated by a clear seismicity gap. On the other hand, the deep LVF and its conjugate fault have hosted fewer small-magnitude seismic events. In the region near the fault plane of the 2024 mainshock (indicated by the magenta and blue dashed lines in Figure 3), the pre-2020 earthquake distribution is sparse, and no distinct fault trace is visible. We label this low-seismicity area as Groups 4 and 5 (Figure 3). Although the historical seismicity in this zone was sparse, our FFI of the 2024 mainshock revealed that this area experienced significant coseismic slip. Along the tectonically complex and seismically active eastern coast of Taiwan, several previous magnitude six earthquakes have involved multiple

faults or segments. For instance, both the 2022 Mw6.5 and 6.9 Chishang earthquakes ruptured the CRF and the LVF in the southern Longitudinal Valley (Yang et al., 2024). Farther north, the 2018 Mw6.4 Hualien earthquake activated both the Meilun Fault and the LVF (Lo et al., 2019). Given the large magnitude of the 2024 mainshock, it is not surprising that the event also ruptured two faults. However, unlike previous events that were confined to shallow depths (<15 km), the primary fault slip during the 2024 mainshock occurred at depths of 20–40 km. This event and its aftershocks thus offer a valuable opportunity for future studies to better constrain the location, geometry, and structure of the deep LVF and the previously unrecognized west-dipping conjugate fault. Understanding these deeper structures will provide important new insights for updating seismic hazard assessments in Hualien and the surrounding region.

5. Conclusion

In this study, we imaged the rupture process and constructed the coseismic slip model for the 2024 Mw7.4 Hualien earthquake using SEBP and FFI techniques. The earthquake involved a complicated rupture process on a conjugate fault system. The geometry of the optimal fault planes, resolved by the joint inversion, aligned with the east-dipping LVF and its west-dipping conjugate fault. The FFI results showed that the rupture initiated on the LVF and propagated north-northeastward and downward. At ∼8 s, the rupture reached the intersection with the conjugate fault, after which slip developed simultaneously on both fault planes. Peak slip amplitudes were ∼3.4 m on the LVF and ∼4.4 m on the conjugate fault. The seismic moment release was partitioned nearly equally, with 47% on the LVF and 53% on the conjugate fault. The total rupture duration was ∼20 s. The occurrence of this event confirms the seismic potential of the LVF, highlighting the need for updated hazard risk evaluations and corresponding mitigation strategies for Hualien and nearby cities.

Data Availability Statement

The MATLAB code of SEBP is available at Xu and Meng (2024). The Python software package Obspy (The ObsPy Development Team, 2025) is used for seismic data requesting and waveform filtering. Figures are produced using Generic Mapping Tools (GMT) (Wessel & Smith, 1998), Obspy, and Matlab. The local strong motion data are downloaded from Central Weather Administration (CWA, 2012). The GNSS data are downloaded from Taiwan Seismological and Geophysical Data Management System (GDMS, https://gdms.cwa.gov.tw/GeophyDownload.php) and Nevada Geodetic Laboratory (NGL, http://geodesy.unr.edu/). The original aftershock catalog is obtained from CWA, GDMS (https://gdms.cwa.gov.tw). All seismic data are downloaded through the IRIS Wilber 3 system (https://ds.iris.edu/wilber3/find_event) and Observatories & Research Facilities for European Seismology (ORFEUS; https://www.orfeus-eu.org/), including the following seismic networks: (a) the AU (Geoscience Australia, 2021); (b) the CZ (Charles University in Prague (Czech) et al., 1973); (c) the EI (Dublin Institute for Advanced Studies, 1993); (d) the FR (Epos-France, 1995); (e) the G (IPGP and EOST, 1982); (f) the GE (GEOFON Data Centre, 1993); (g) the GR (Federal Institute for Geosciences and Natural Resources, 1976); (h) the GU (University of Genoa, 1967); (i) the II (Scripps Institution of Oceanography, 1986); (j) the IU (GSN; Albuquerque Seismological Laboratory (ASL)/USGS, 1988); (k) the IV (INGV Seismological Data Centre, 2006); (l) the MN (MedNet Project Partner Institutions, 1990); (m) the ND (New Caledonian Seismic Network And RESIF Datacenter, 2009); (n) the NL (KNMI, 1993); (o) the OE (ZAMG, 1987); (p) the OX (OGS, 2016); (q) the S1 (Salmon et al., 2011); (r) the TA (Transportable Array; IRIS, 2003); (s) the TH (Institut fuer Geowissen-schaften, Friedrich-Schiller-Universitaet Jena, 2009); (t) the US (Albuquerque Seismological Laboratory (ASL)/USGS, 1990).

Acknowledgments

We thank Hsin-Hua Huang for providing the velocity model. We thank Chen Ji for the fruitful discussion. We thank Editor Dr. Germán Prieto and two anonymous reviewers for their valuable suggestions that improved the manuscript. We thank GDMS of CWA and Nevada Geodetic Laboratory for releasing the GNSS data. We thank GDMS of CWA for releasing the strong motion data. We thank National Taiwan University for releasing the seismicity catalog. This work contains modified Copernicus data from the Sentinel-1 satellite provided by the European Space Agency. Liuwei Xu and Lingsen Meng are supported by the NSF CAREER Grant (EAR-1848486) and the Leon and Joanne V.C.Knopoff Fund. Yen-Yu Lin is supported by "Earthquake-Disaster & Risk Evaluation and Management Center, E-DREaM" from The Featured Areas Research Center Program within the framework of the Higher Education Sprout Project by the Ministry of Education in Taiwan, and funded through the National Science and Technology Council with Grant 113-2116-M-008-007-.

References

Abrahamson, N. A., & Somerville, P. G. (1996). Effects of the hanging wall and footwall on ground motions recorded during the Northridge earthquake. *Bulletin of the Seismological Society of America*, *86*(1B), S93–S99. https://doi.org/10.1785/BSSA08601B0S93

Albuquerque Seismological Laboratory (ASL)/USGS. (1990). United States National Seismic Network [Dataset]. *International Federation of Digital Seismograph Networks*. https://doi.org/10.7914/SN/US

Albuquerque Seismological Laboratory (ASL)/USGS. (1988). Global Seismograph Network (GSN—IRIS/USGS) [Dataset]. *International Federation of Digital Seismograph Networks*. https://doi.org/10.7914/SN/IU

Central Weather Administration (CWA, Taiwan). (2012). Central weather administration seismographic network [Dataset]. *International Federation of Digital Seismograph Networks*. https://doi.org/10.7914/SN/T5

Charles University in Prague (Czech), Institute of Geonics, Institute of Geophysics, Academy of Sciences of the Czech Republic, Institute of Physics of the Earth Masaryk University (Czech), & Institute of Rock Structure and Mechanics. (1973). Czech Regional Seismic Network [Dataset]. *International Federation of Digital Seismograph Networks*. https://doi.org/10.7914/SN/CZ

Cheloni, D., Famiglietti, N. A., Caputo, R., Tolomei, C., & Vicari, A. (2024). A composite fault model for the 2024 MW 7.4 Hualien earthquake sequence in eastern Taiwan inferred from GNSS and InSAR data. *Geophysical Research Letters*, *51*(20), e2024GL110255. https://doi.org/10.1029/2024GL110255

Chen, K. H., Toda, S., & Rau, R.-J. (2008). A leaping, triggered sequence along a segmented fault: The 1951 ML 7.3 Hualien-Taitung earthquake sequence in eastern Taiwan. *Journal of Geophysical Research*, *113*(B2), B02304. https://doi.org/10.1029/2007JB005048

Cheng, S.-N., Yu, T.-T., Yeh, Y.-T., & Chang, Z.-S. (1997). Relocation of the 1951 Hualien, Taitung earthquake sequence, in Weather analysis and forecasting, proceedings of marine meteorology and seismology. In *Commemoration of 100 Years of Weather Observation in the Taiwan Area, Taipei City, Taiwan* (pp. 690–699).

Ching, K. E., Rau, R. J., & Zeng, Y. (2007). Coseismic source model of the 2003 Mw 6.8 Chengkung earthquake, Taiwan, determined from GPS measurements. *Journal of Geophysical Research*, *112*(B6). https://doi.org/10.1029/2006JB004439

Dublin Institute for Advanced Studies. (1993). Irish National Seismic Network [Dataset]. *International Federation of Digital Seismograph Networks*. https://doi.org/10.7914/SN/EI

Epos-France. (1995). Epos-France Broad-Band Network (RLBP) [Dataset]. *Epos-France Seismological Data Centre*. https://doi.org/10.15778/resif.fr

Federal Institute for Geosciences Natural Resources. (1976). German Regional Seismic Network (GRSN) [Dataset]. *Other/Seismic Network*. https://doi.org/10.25928/mbx6-hr74

GEOFON Data Centre. (1993). GEOFON seismic network [Dataset]. *GFZ Data Services Other/Seismic Network*. https://doi.org/10.14470/TR560404

Geoscience Australia. (2021). Australian National Seismograph Network Data Collection (version 2.0, September 2018) [Dataset]. *Commonwealth of Australia*. https://doi.org/10.26186/144675

Hsu, Y.-J., Yu, S.-B., Simons, M., Kuo, L.-C., & Chen, H.-Y. (2009). Interseismic crustal deformation in the Taiwan plate boundary zone revealed by GPS observations, seismicity, and earthquake focal mechanisms. *Tectonophysics*, *479*(1–2), 4–18. https://doi.org/10.1016/j.tecto.2008.11.016

Hu, J. C., Cheng, L. W., Chen, H. Y., Wu, Y. M., Lee, J. C., Chen, Y. G., et al. (2007). Coseismic deformation revealed by inversion of strong motion and GPS data: The 2003 Chengkung earthquake in eastern Taiwan. *Geophysical Journal International*, *169*(2), 667–674. https://doi.org/10.1111/j.1365-246X.2007.03359.x

Huang, H.-H., & Wang, Y. (2022). Seismogenic structure beneath the northern Longitudinal Valley revealed by the 2018–2021 Hualien earthquake sequences and 3-D velocity model. *Terrestrial, Atmospheric and Oceanic Sciences*, *33*(1), 17. https://doi.org/10.1007/s44195-022-00017-z

Huang, H.-H., Wu, Y.-M., Song, X., Chang, C.-H., Lee, S.-J., Chang, T.-M., & Hsieh, H.-H. (2014). Joint Vp and Vs tomography of Taiwan: Implications for subduction-collision orogeny. *Earth and Planetary Science Letters*, *392*, 177–191. https://doi.org/10.1016/j.epsl.2014.02.026

Huang, M. H., & Huang, H. H. (2018). The complexity of the 2018 Mw 6.4 Hualien earthquake in east Taiwan. *Geophysical Research Letters*, *45*(24), 13–249. https://doi.org/10.1029/2018GL080821

Hwang, L., & Kanamori, H. (1989). Teleseismic and strong-motion source spectra from two earthquakes in eastern Taiwan. *Bulletin of the Seismological Society of America*, *79*(4), 935–944. https://doi.org/10.1785/BSSA0790040935

INGV Seismological Data Centre. (2006). Rete Sismica Nazionale (RSN) [Dataset]. *Istituto Nazionale di Geofisica e Vulcanologia (INGV)*. https://doi.org/10.13127/SD/X0FXNH7QFY

Institut fuer Geowissenschaften, Friedrich-Schiller-Universitaet Jena. (2009). Thüringer Seismologisches Netz [Dataset]. *International Federation of Digital Seismograph Networks*. https://doi.org/10.7914/SN/TH

Institut de Physique du Globe de Paris (IPGP) and Ecole et Observatoire des Sciences de la Terre de Strasbourg (EOST). (1982). GEOSCOPE, French global network of broad band seismic stations [Dataset]. *Institut de Physique du Globe de Paris (IPGP)*. https://doi.org/10.18715/GEOSCOPE.G

IRIS Transportable Array. (2003). USArray transportable array [Dataset]. *International Federation of Digital Seismograph Networks*. https://doi.org/10.7914/SN/TA

Ishii, M., Shearer, P. M., Houston, H., & Vidale, J. E. (2005). Extent, duration, and speed of the 2004 Sumatra-Andaman earthquake imaged by the Hi-Net array. *Nature*, *435*(7044), 933–936. https://doi.org/10.1038/nature03675

Istituto Nazionale di Oceanografia e di Geofisica Sperimentale—OGS. (2016). North-East Italy seismic network [Dataset]. *FDSN*. https://doi.org/10.7914/SN/OX

Ji, C., Helmberger, D. V., Wald, D. J., & Ma, K.-F. (2003). Slip history and dynamic implications of the 1999 Chi-Chi, Taiwan, earthquake. *Journal of Geophysical Research*, *108*, 2412. https://doi.org/10.1029/2002JB001764

Ji, C., Wald, D. J., & Helmberger, D. V. (2002). Source description of the 1999 Hector Mine, California, earthquake, part I: Wavelet domain inversion theory and resolution analysis. *Bulletin of the Seismological Society of America*, *92*(4), 1192–1207. https://doi.org/10.1785/0120000916

Jian, P.-R., Liang, W.-T., & Kuo, B.-Y. (2022). Three-dimensional stress model of the collision-subduction junction east of Taiwan: Implications for the decoupling of the Luzon Arc during subduction. *Journal of Geophysical Research: Solid Earth*, *127*(9), e2022JB024054. https://doi.org/10.1029/2022JB024054

Jian, P.-R., & Wang, Y. (2022). Applying unsupervised machine-learning algorithms and MUSIC back-projection to characterize 2018–2022 Hualien earthquake sequence. *Terrestrial, Atmospheric and Oceanic Sciences*, *33*(1), 28. https://doi.org/10.1007/s44195-022-00026-y

Kao, H., Shen, S.-J., & Ma, K.-F. (1998). Transition from oblique subduction to collision: Earthquakes in the southernmost Ryukyu arc-Taiwan region. *Journal of Geophysical Research*, *103*(B4), 7211–7229. https://doi.org/10.1029/97JB03510

Kiser, E., & Ishii, M. (2017). Back-projection imaging of earthquakes. *Annual Review of Earth and Planetary Sciences*, *45*(1), 271–299. https://doi.org/10.1146/annurev-earth-063016-015801

KNMI. (1993). Netherlands seismic and acoustic network [Dataset]. *Royal Netherlands Meteorological Institute (KNMI) Other/Seismic Network*. https://doi.org/10.21944/e970fd34-23b9-3411-b366-e4f72877d2c5

Kuo, C., Huang, J., Lin, C., Hsu, T., Chao, S., & Wen, K. (2018). Strong ground motion and pulse-like velocity observations in the near-fault region of the 2018 Mw 6.4 Hualien, Taiwan, Earthquake. *Seismological Research Letters*, *90*(1), 40–50. https://doi.org/10.1785/0220180195

Lee, S. J., Lin, T. C., Liu, T. Y., & Wong, T. P. (2019). Fault-to-fault jumping rupture of the 2018 Mw 6.4 Hualien earthquake in eastern Taiwan. *Seismological Research Letters*, *90*(1), 30–39. https://doi.org/10.1785/0220180182

Lo, C.-L., Chang, E. T.-Y., & Chao, B. F. (2013). Relocating the historical 1951 Hualien earthquake in eastern Taiwan based on tide gauge record. *Geophysical Journal International*, *192*(2), 854–860. https://doi.org/10.1093/gji/ggs058

Lo, Y.-C., Yue, H., Sun, J., Zhao, L., & Li, M. (2019). The 2018 Mw6.4 Hualien earthquake: Dynamic slip partitioning reveals the spatial transition from mountain building to subduction. *Earth and Planetary Science Letters*, *524*, 115729. https://doi.org/10.1016/j.epsl.2019.115729

MedNet Project Partner Institutions. (1990). Mediterranean Very Broadband Seismographic Network (MedNet) [Dataset]. *Istituto Nazionale di Geofisica e Vulcanologia (INGV)*. https://doi.org/10.13127/SD/FBBBTDTD6Q

Meng, L., Inbal, A., & Ampuero, J.-P. (2011). A window into the complexity of the dynamic rupture of the 2011 Mw 9 Tohoku-Oki earthquake. *Geophysical Research Letters*, *38*(7), L00G07. https://doi.org/10.1029/2011GL048118

Meng, L., Zhang, A., & Yagi, Y. (2016). Improving back projection imaging with a novel physics-based aftershock calibration approach: A case study of the 2015 Gorkha earthquake. *Geophysical Research Letters*, *43*(2), 628–636. https://doi.org/10.1002/2015GL067034

New Caledonian Seismic Network And RESIF Datacenter. (2009). The New Caledonian seismic network [Dataset]. *RESIF - Réseau Sismologique et géodésique Français*. https://doi.org/10.15778/RESIF.ND

Qiu, J., Ji, L., Zhu, L., Li, Y., Liu, C., & Zhao, Q. (2024). Coseismic deformation and seismogenic structure of the 2024 Hualien Earthquake measured by InSAR and GNSS. *Earthquake Research Advances*, *5*(1), 100328. https://doi.org/10.1016/j.eqrea.2024.100328

Salmon, M., Balfour, N., Sambridge, M., Mousavi, S., & Pickle, R. (2011). Australian seismometers in schools [Dataset]. *AusPass*. https://doi.org/10.7914/SN/S1

Scripps Institution of Oceanography. (1986). Global Seismograph Network—IRIS/IDA [Dataset]. *International Federation of Digital Seismograph Networks*. https://doi.org/10.7914/SN/II

Shyu, J. B. H., Chung, L.-H., Chen, Y.-G., Lee, J.-C., & Sieh, K. (2007). Re-evaluation of the surface ruptures of the November 1951 earthquake series in eastern Taiwan, and its neotectonic implications. *Journal of Asian Earth Sciences*, *31*(3), 317–331. https://doi.org/10.1016/j.jseaes.2006.07.018

Stein, R. S., Toda, S., Chan, C.-H., & Sevilgen, V. (2024). Magnitude 7.4 shock ruptures a fault in the Longitudinal Valley of eastern Taiwan, Temblor. https://doi.org/10.32858/temblor.338

Styron, R., & Pagani, M. (2020). The GEM global active faults database. *Earthquake Spectra*, *36*(1_suppl), 160–180. https://doi.org/10.1177/8755293020944182

Tang, X., Guo, R., Li, L., Xu, Y., Xu, J., Zheng, Y., & Sun, H. (2024). Earthquake Interactions in Eastern Taiwan: Insight from the 2024 Mw 7.3 Hualien earthquake. *Seismological Research Letters*, *XX*, 1–10. https://doi.org/10.1785/0220240230

The ObsPy Development Team. (2025). ObsPy 1.4.2 (1.4.2) [Software]. *Zenodo*. https://doi.org/10.5281/zenodo.15309143

University of Genoa. (1967). Regional seismic network of North Western Italy [Dataset]. *International Federation of Digital Seismograph Networks*. https://doi.org/10.7914/SN/GU

Waldhauser, F., & Ellsworth, W. L. (2000). A double-difference earthquake location algorithm: Method and application to the Northern Hayward Fault, California. *Bulletin of the Seismological Society of America*, *90*(6), 1353–1368. https://doi.org/10.1785/0120000006

Wessel, P., & Smith, W. H. F. (1998). New, improved version of generic mapping tools released. *Eos, Transactions American Geophysical Union*, *79*(47), 579. https://doi.org/10.1029/98EO00426

Wu, Y. M., Chang, C. H., Kuo-Chen, H., Hunag, H. H., Wang, C. Y., Aaa, A., & Aaa, A. (2013). On the use of explosion records for examining earthquake location uncertainty in Taiwan. *Terrestrial, Atmospheric and Oceanic Sciences*, *24*(4–2), 685–694. https://doi.org/10.3319/TAO.2013.01.31.01(T)

Xu, L., & Meng, L. (2024). Codes for Slowness-Enhanced Back-Projection (SEBP) [Dataset]. *Zenodo*. https://doi.org/10.5281/zenodo.12801968

Yang, Y.-H., Li, L., Hu, J.-C., Tung, H., Xu, Q., Li, X., et al. (2024). Double-Vergent plate boundary faults and triggered coseismic rupture of the 2022 Chihshang doublet earthquake occurred in eastern Taiwan. *Seismological Research Letters*, *95*(4), 2081–2091. https://doi.org/10.1785/0220230026

ZAMG—Zentralanstalt für Meterologie und Geodynamik. (1987). Austrian seismic network [Dataset]. *International Federation of Digital Seismograph Networks*. https://doi.org/10.7914/SN/OE

Zhang, A. (2019). *Theories and applications of enhanced earthquake back-projection imaging*. eScholarship, University of California.

Zheng, A., Yu, X., Bai, C., Xu, W., Qian, J., Zhang, W., & Chen, X. (2024). Thrust-dominated unilateral rupture of a blind listric fault associated with the 2024 Hualien earthquake. *Scientific Reports*, *14*(1), 31496. https://doi.org/10.1038/s41598-024-82971-x

Zheng, T.-Y., Yao, Z.-X., & Liu, P.-C. (1995). The 14 November 1986 Taiwan earthquake—An event with isotropic component. *Physics of the Earth and Planetary Interiors*, *91*(4), 285–298. https://doi.org/10.1016/0031-9201(95)03019-S

Zhu, L., & Rivera, L. A. (2002). A note on the dynamic and static displacements from a point source in multilayered media. *Geophysical Journal International*, *148*(3), 619–627. https://doi.org/10.1046/j.1365-246X.2002.01610.x

References From the Supporting Information

Dong, D.-N., & Bock, Y. (1989). Global Positioning System Network analysis with phase ambiguity resolution applied to crustal deformation studies in California. *Journal of Geophysical Research*, *94*(B4), 3949–3966. https://doi.org/10.1029/JB094iB04p03949

Geng, J., Chen, X., Pan, Y., Mao, S., Li, C., Zhou, J., & Zhang, K. (2019). PRIDE PPP-AR: An open-source software for GPS PPP ambiguity resolution. *GPS Solutions*, *23*(4), 91. https://doi.org/10.1007/s10291-019-0888-1

Geng, J., Zhang, Q., Li, G., Liu, J., & Liu, D. (2022). Observable-specific phase biases of Wuhan multi-GNSS experiment analysis center's rapid satellite products. *Satellite Navigation*, *3*(1), 23. https://doi.org/10.1186/s43020-022-00084-0

Lee, S.-J., Huang, H.-H., Shyu, J. B. H., Yeh, T.-Y., & Lin, T.-C. (2014). Numerical earthquake model of the 31 October 2013 Ruisui, Taiwan, earthquake: Source rupture process and seismic wave propagation. *Journal of Asian Earth Sciences*, *96*, 374–385. https://doi.org/10.1016/j.jseaes.2014.09.020

Lee, S. J., Wong, T. P., Liu, T. Y., Lin, T. C., & Chen, C. T. (2020). Strong ground motion over a large area in northern Taiwan caused by the northward rupture directivity of the 2019 Hualien earthquake. *Journal of Asian Earth Sciences*, *192*, 104095. https://doi.org/10.1016/j.jseaes.2019.104095